ARMY RESEARCH LABORATORY

Detection of Bioaerosols using Single Particle Thermal Emission Spectroscopy

by Dr. Kristan P. Gurton, Mr. Melvin Felton, and Dr. Pan Yongle

NOTICES

Disclaimers

The findings in this report are not to be construed as an official Department of the Army position unless so designated by other authorized documents.

Citation of manufacturer's or trade names does not constitute an official endorsement or approval of the use thereof.

Destroy this report when it is no longer needed. Do not return it to the originator.

Army Research Laboratory

Adelphi, MD 20783-1197

ARL-TR-6365   **March 2013**

Detection of Bioaerosols using Single Particle Thermal Emission Spectroscopy

Dr. Kristan P. Gurton, Mr. Melvin Felton, and Dr. Pan Yongle
Computational and Information Sciences Directorate, ARL

REPORT DOCUMENTATION PAGE				*Form Approved* *OMB No. 0704-0188*
Public reporting burden for this collection of information is estimated to average 1 hour per response, including the time for reviewing instructions, searching existing data sources, gathering and maintaining the data needed, and completing and reviewing the collection information. Send comments regarding this burden estimate or any other aspect of this collection of information, including suggestions for reducing the burden, to Department of Defense, Washington Headquarters Services, Directorate for Information Operations and Reports (0704-0188), 1215 Jefferson Davis Highway, Suite 1204, Arlington, VA 22202-4302. Respondents should be aware that notwithstanding any other provision of law, no person shall be subject to any penalty for failing to comply with a collection of information if it does not display a currently valid OMB control number. **PLEASE DO NOT RETURN YOUR FORM TO THE ABOVE ADDRESS.**				
1. REPORT DATE *(DD-MM-YYYY)* March 2013	**2. REPORT TYPE** DRI		**3. DATES COVERED (From - To)** December 19 1012	
4. TITLE AND SUBTITLE Detection of Bioaerosols using Single Particle Thermal Emission Spectroscopy			**5a. CONTRACT NUMBER**	
			5b. GRANT NUMBER	
			5c. PROGRAM ELEMENT NUMBER	
6. AUTHOR(S) Dr. Kristan P. Gurton, Mr. Melvin Felton, and Dr. Pan Yongle			**5d. PROJECT NUMBER**	
			5e. TASK NUMBER	
			5f. WORK UNIT NUMBER	
7. PERFORMING ORGANIZATION NAME(S) AND ADDRESS(ES) U.S. Army Research Laboratory ATTN: RDRL-CIE-S 2800 Powder Mill Road Adelphi, MD 20783-1197			**8. PERFORMING ORGANIZATION REPORT NUMBER** ARL-TR-6365	
9. SPONSORING/MONITORING AGENCY NAME(S) AND ADDRESS(ES)			**10. SPONSOR/MONITOR'S ACRONYM(S)**	
			11. SPONSOR/MONITOR'S REPORT NUMBER(S)	
12. DISTRIBUTION/AVAILABILITY STATEMENT Approved for public release; distribution unlimited.				
13. SUPPLEMENTARY NOTES				
14. ABSTRACT This report documents current finding for an ongoing study designed to assess the ability to measure *in situ* the absorption spectra from a single bio-aerosol particle. In particular, we describe experimental method(s) and techniques capable of detecting the single particle thermal emission in the infrared (IR) spectral range from 3 to 12 µm. We report current findings to accurately measure the graybody spectral emission from a 1–20 micron-size bioparticle when heated to temperatures in excess of a 100 °C. Prevailing theory suggests a strong link between thermal emission and absorption spectra for bulk materials held at elevated temperatures. This study (1) establishes whether it is possible to measure and spectrally resolve the thermal emission from a small optically heated aerosol-type particle, and (2) determines the functional relationship(s) that couple the measured thermal emission with actual absorption.				
15. SUBJECT TERMS: Aerosol, absorption, chemical and biological weapon, anthrax, spectroscopy, thermal emission, single particle, Director's Research Initiative (DRI)				
16. SECURITY CLASSIFICATION OF:			**17. LIMITATION OF ABSTRACT** UU	**18. NUMBER OF PAGES** 28	**19a. NAME OF RESPONSIBLE PERSON** Kristan P. Gurton
a. REPORT Unclassified	**b. ABSTRACT** Unclassified	**c. THIS PAGE** Unclassified			**19b. TELEPHONE NUMBER** *(Include area code)* (301) 394-2093

Contents

List of Figures

1. Background

The motivation for this study was to investigate whether we could directly measure a uniquely identifiable physical parameter for a small, single, aerosol particle, which could then be used to reliably detect the presence of airborne biological warfare (BW) agents at trace levels. Currently, there are no reliable means of accurate "real-time" detection and identification of hazardous biological aerosols. Existing detection methods typically involve collection of bioaerosols on filters of sufficient mass and subsequent chemical analysis by fluorescent antibody tagging. Although fairly reliable, these techniques require relatively long periods of time to process and analyze. Such systems also require an a priori "guess" as to what specific antibodies should be considered. As a result, these biochemical based systems are easily thwarted by choosing a slightly atypical agent or variant biological species.

If the rapid detection and identification of BW agents is a primary goal, then direct optical probing should be considered. Examples of current state-of-the-art optical methods include two-dimensional (2-D) elastic scattering, Raman scattering, laser induced breakdown spectroscopy (LIBS), and fluorescent spectroscopy (*1–6*). Although Raman and fluorescent spectroscopy have shown some promise in detecting differences among certain strains of bacteria, these results are often contingent on the biological samples being extremely clean and devoid of any growth media, i.e., spectroscopically pure.

In addition, many of these optical based methods are strongly affected by differences in particle shape and size (*7, 8*). This is particularly problematic since it is well known that bioaerosol particles are often made up of agglomerated sub-particles and possess no particular preferential shape. In contrast, the approach proposed here, i.e., to measure qualitatively an absorption related parameter, is relatively unaffected by changes in particle shape and/or size.

2. Theory

It is well known that the thermal emission that radiates from a small particle depends on two physical parameters, i.e., the temperature and the emission cross section (*9–11*). Equation 1 shows the spectral intensity, δI_λ, emitted by a small particle of unit to be

$$\delta I_\lambda = \varepsilon(\lambda) R_b(\lambda, T_p) \tag{1}$$

where $\varepsilon(\lambda)$ is the particle spectral emissivity cross section and $R_b(\lambda, T_p)$ is the Planck function, i.e., the radiance flux from a blackbody at temperature T_p[*]. According to the generalized Kirchhoff's law, the emission cross section for an arbitrary object at a given temperature is equivalent to the absorption cross section at the same wavelength, except the direction of the radiant flux is reversed[†] (14).

Van De Hulst (12) and Bohren (13) extend the Kirchhoff relationship to small arbitrarily shaped aerosol particles and state that a measure of the emission cross section, $\varepsilon(\lambda)$ yields the same microphysical properties as the absorption cross section, $\alpha(\lambda)$. However, as pointed out by Bohren and Hottel et al., the assertion that the thermal system(s) must be in thermal equilibrium for Kirchhoff's law to be valid is not entirely accurate. As a result, Kirchhoff relationships are still valid for "non-equilibrium" systems so long as they are characterized as a thermal "graybody" system, i.e., emissivity less than 1. Hottel shows that for a graybody, the Kirchhoff relationships that link the spectral emissivity to spectral absorptivity are still valid even if the particle is not in thermal equilibrium, so long as the absorption cross section is not unduly affected by changes in temperature[†].

Additional information about the structural nature of the particle may be inferred by considering the rate in which a heated particle dissipates thermal energy during a cooling cycle. A measure of the so-called "characteristic cooling time," τ, refers to the time period required for a particle to transfer a fraction of its internal heat to the surrounding gas. Thus, for a given size particle, the rate in which the particle cools is a direct measure of whether the structure is solid, liquid, or amorphous (11, 14).

To understand this, it is instructive to identify all of the possible mechanisms involved in particle cooling after it has been heated to some temperature, T_p, above the surrounding gas temperature, T_g. There are three processes which cause cooling: (1) heat transfer to the surrounding gas, (2) heat energy lost due to radiation, and (3) particle evaporation. The total heat flux from the particle in the free molecular regime is given by the three terms in the following equation,

$$\dot{q} = 4\pi a^2 \frac{1}{2} p_g c_t \left(\frac{T_p}{T_g} - 1\right) + 4\pi a^2 \varepsilon \sigma \left(T_p{}^4 - T_g{}^4\right) + 4\pi a^2 G_v \Delta h, \qquad (2)$$

$$c_t = \sqrt{\frac{8kT_g}{\pi m_g}} , \qquad (3)$$

---

[*]In general the emissivity is a function of wavelength, direction, and temperature, but for the case at hand we will assume modest temperatures, well below ionization, and that the radiance is captured over a sufficiently large enough solid angle as to reduce directional variation.

[†]One of the most thorough descriptions involving the often miss-used derivation of Kirchhoff's law can be found in H. C. Hottel, A.F. Sarofim, *Radiative Transfer*, McGraw Hill, New York, 1967, pp. 4–24.

where p_g is the gas pressure, m_g and c_t are the mass and average velocity of the gas molecules, ε is the total particle emissivity, k and σ are the Boltzmann and Stefan-Boltzmann constants, G_v is the flux density of vapor leaving the particle, and Δh is the specific heat of evaporation. The first term on the right-hand side of equation 2 represents the heat of conductivity in a free-molecular regime with the assumption of diffuse reflection of gas molecules at the particle surface (*15*). The second and third terms represent heat loss due to radiation and evaporation, respectively, and are assumed small so long as the particle heating is kept moderate (a condition that can be relaxed later).

We now consider a typical energy balance equation for the cooling cycle of a particle after the heat source is removed. The rate at which the particle cools is given by equation 4:

$$m_p c_p \frac{dT_p}{dt} = -\dot{q} , \tag{4}$$

where T_p is the instantaneous temperature of the particle, m_p is the mass of the particle, and c_p is the specific heat of the particle. Combining equations 4 and 2 and integrating over time, t, we find the solution corresponding to particle temperature $T_p(t)$ has the form

$$\frac{T_p - T_g}{T_g} = \left(\frac{T_p^0}{T_g} - 1 \right) exp^{\left(-\frac{t}{\tau} \right)} . \tag{5}$$

where T_p^0 is the initial temperature at t=0, and the reservoir of surrounding gas is assumed large enough so that T_g remains constant. The parameter τ is taken to be the characteristic cooling period for the particle due to heat transfer to the surrounding gas. To get an idea of the magnitude for the possible values of τ, we consider a glycerin particle of varying diameters, with the following physical parameters: mass-density, $\rho_p =1.27$ (kg/m^3), thermal conductivity, K= 0.29 (W/mK), and a specific heat value of $c_p = 2.43$ (kJ/kg*K).

Fourier heat-conduction calculations are conducted in which the characteristic cooling period is plotted as a function of particle radius based on the final condition, $\frac{T_p - T_g}{T_g} = 0.90$, i.e., the particle has cooled to within 10% of the ambient surrounding gas temperature, see figure 1 (*16*).
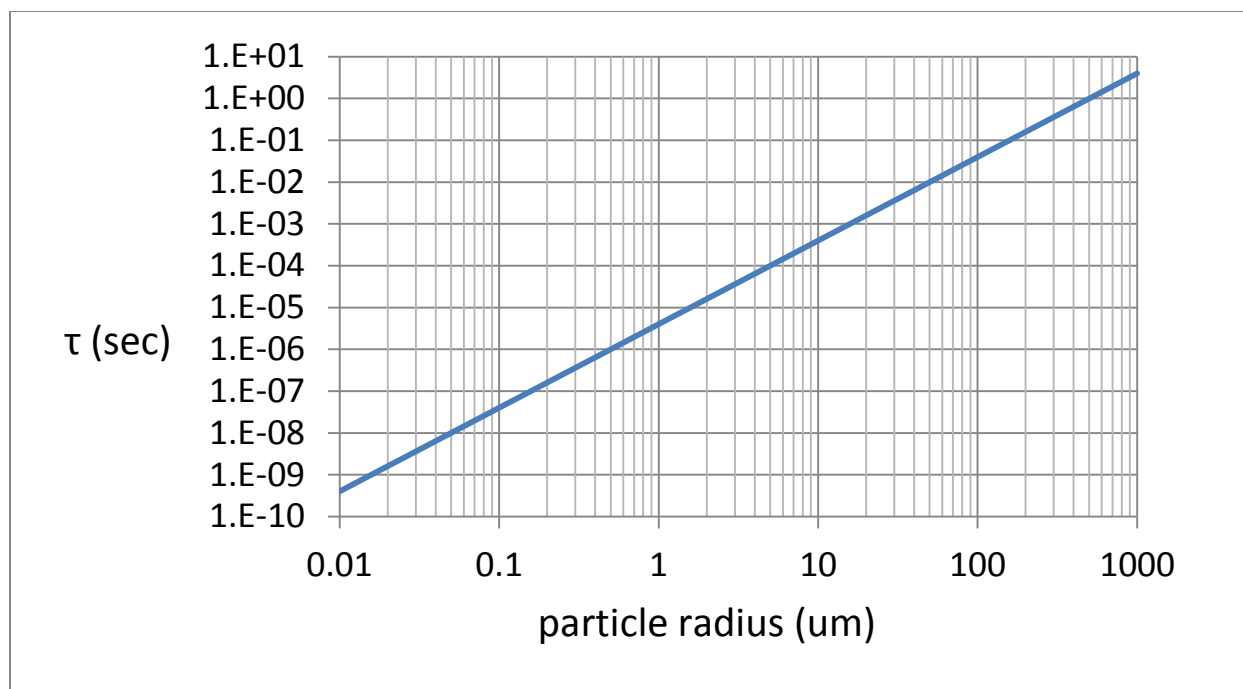
Figure 1. Plot of the characteristic cooling period, τ (sec), for a spherical glycerin particle heated to some initial temperature T_p, and T_g is the temperature of the surrounding gas, where τ has been calculated for the condition $\frac{T_p - T_g}{T_g} = 0.90$.

The desired range of particle diameters for our study is expected to be between 1–30 µm. Based on the results calculated for glycerin shown in figure 1, the anticipated characteristic cooling periods range from approximately 1.0 µs to 10.0 ms. The minimum signal capture periods for the detector system used here, i.e., a time-gated 32 element linear mercury cadmium telluride (MCT) array, is 10 µs. Based on these parameters, it is possible to temporally resolve multiple emission measurements as the particle cools, which would allow for a direct measure of characteristic cooling period, τ, and should provide additional "structural" information about the particle. Then, it is our hope that when coupled with the measured absorption/emission infrared (IR) spectra, this novel/new set of information will be shown to improve our ability to detect and identify harmful bioaerosols at trace levels.

At the time of this writing, we were still in the process of getting our laboratory certified as a bio-safety level 1 (BL1) facility, which is necessary to allow us to aerosolize particulate bio-materials. Although this limited the type of materials we could consider for this proof-of-concept study, there did exist a variety of good, safe, and most importantly, representative class of organic compounds that we could use.

We chose to use common mineral oil as a surrogate bio-compound for the following reasons. First, mineral oil possesses a large macro-molecular structure similar to the chemical structures seen in amino acids and simple proteins. Because mineral oil is made up of a long chain of alkanes in the C15 to C40 range, it is known to exhibit three distinctive main absorption bands in

the midIR spectral range that we could key on in our analysis. Second, mineral oil has the low vapor pressure required to resist phase change (evaporation) when heated to temperatures in excess of 100 °C. Finally, and most important, it is our belief that the results shown here using liquid mineral oil will be directly applicable for future studies in which actual bioaerosols are considered. It is our assertion that any method that can detect the emission spectra from a liquid droplet should be effective when applied to bioaerosols.

3. Experiment

During our first year, we considered multiple particle "trapping" techniques that would allow us to capture and hold in place a single test particle for long periods of optical probing. Because of anticipated difficulty in measuring minute quantities of radiant flux from a modestly heated micron-size particle, we believed that single particle trapping offered the best opportunity to integrate the expected small signal for as long as necessary.

To accomplish this, various acoustic and optical based techniques designed to trap and suspend a single particle where designed, assembled, and tested. Tests using acoustic trapping techniques were ineffective for this study since the method was limited to stable suspension of large particles only, e.g., spherical particles with diameters on the order of 500 µm and above.

Optical techniques that involve laser based trapping were considered next, i.e., forces generated by radiative pressure and photopheresis. Tests involving radiative pressure proved to be relatively weak when compared to particle trapping using the photophoretic force (*17–19*). Test results routinely showed the photophoretic force to be several orders of magnitude greater than the radiative force technique pioneered by Ashkin et al. (*20*).

In general, photophoretic trapping occurs when a moderately absorbing particle is positioned within a null field intensity region of a focused laser, i.e., a small volume in which the intensity is a minimum surrounded by regions of high intensity. There are two types of photophoretic generated forces, indirect-positive and indirect-negative (figure 2).
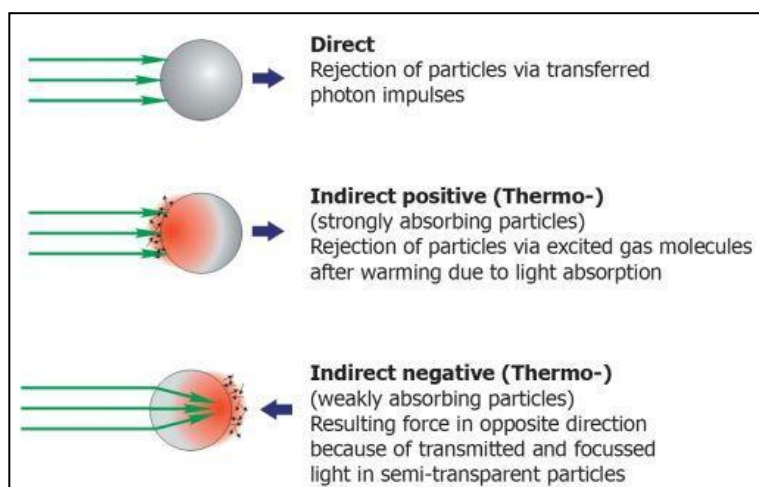
Figure 2. Examples of optical induced forces on small particles.

Indirect-positive force occurs when an absorbing particle enters a null optical region and migrates toward a volume of high intensity. Optical absorption occurs on the leading edge of the particle resulting in non-uniform heating. Kinetic energy is then transferred from surrounding gas molecules to the particle, exerting a net force that pushes the particle back towards a low intensity region. Indirect-negative force occurs for refractive non-absorbing particles. When a refractive particle enters the null region and migrates to a region of high optical intensity, a portion of the energy is refracted (focused) through the particle and causes localized heating on the far side of the particle. This, in turn, generates a net force that pushes the particle back into the center of the void. In either case, the particle is effectively trapped when the dimension of the void and particle are approximately the same. There are many methods in the literature describing how to generate laser induced null fields appropriate for photophoretic trapping, some more complex than others, e.g., bottle-beam trapping, vortex beam trapping, and Bessel beam trapping (*21–23*).

We found the simplest and most stable means for generating null field points is to focus a collimated laser with an uncorrected spherical lens, i.e., by inducing common spherical aberration. When parallel rays aligned with the optical axis are focused using a spherical lens, marginal rays (rays near the edges of the lens) focus at slightly different points along the optical axis than rays that enter near the lens center (figure 3a). This results in "hot" and "cold" points along the optical axis in which a particle can be trapped.

By using the output of a focused 50-mW helium neon (HeNe) laser we were able to trap a wide variety of absorbing and refractive particles. After much trial and error, we determined that two basic conditions were necessary for successful trapping: (1) the particle (or agglomerate) must have relatively low thermal diffusivity so that asymmetric particle heating can occur, and (2) the dimensions of the particle must match that of the optical void(s) created by the aberration. Particle materials successfully trapped include carbon, silica, ragweed pollen, albumin, and agglomerated *bacillus subtilis* (BG) endospores.
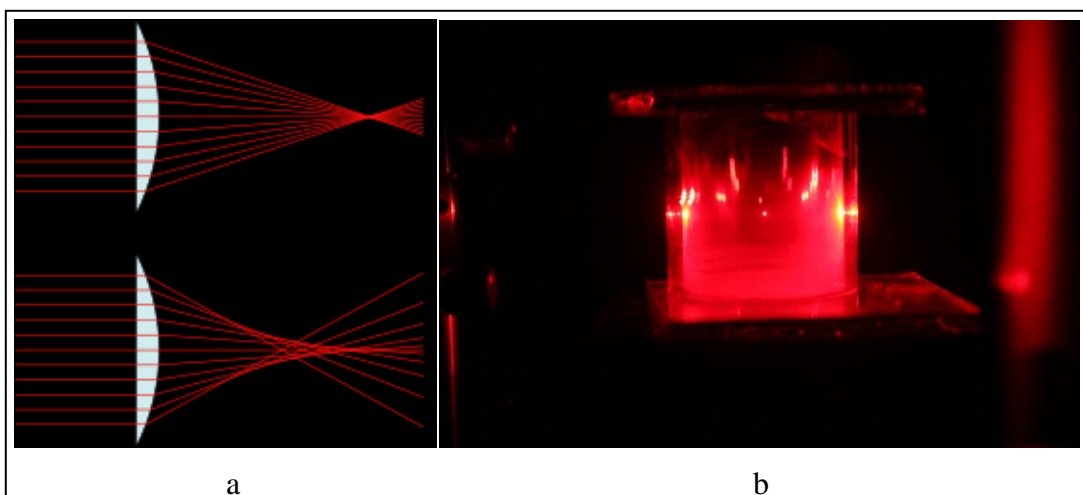
Figure 3. (a) The top image shows a well defined focal spot for a spherically "corrected" lens and the bottom image shows the resultant trapping region(s) located along the optical axis that occur when an uncorrected spherical lens is used to focus a laser beam. (b) A photograph of a 15-μm-diameter stably trapped BG endospore using photophoretic force generated by a focused 50-mW HeNe laser.

Unfortunately, these photophoretic trapping forces were reduced (or eliminated) completely once attempts to optically heat the particle with a secondary carbon dioxide (CO_2) laser were conducted. Early on, we had recognized that external heating of the particle might alter the balance of photophoretic forces, but to what extent was unknown. We had hoped that the photophoretic forces were great enough to withstand a modest (and uniform) rise in temperature. Unfortunately, that was not the case and trapping of all particle types failed as soon as external heating was introduced.

We immediately transitioned to a "free-flowing" type arrangement in which test particles were generated and transported to a specific point in space for optical probing. A simple schematic highlighting the key components for arrangement is shown in figure. 4. The diagram shows a conventional free-flowing particle delivery system similar to that described by Pan et al. (24). In figure 4, test particles are transported and focused to a sample volume of approximately 300 μm^3 using a two isokinetically matched transport nozzles, one for focusing the stream of particles into the sample region and one to capture and collect the particles after optical probing has occurred (25).

Because the radiant flux from a moderately heated micron-size particle is expected to be extremely small, i.e., on the order of tens of nanowatts, great care was taken to (1) optimize signal capture by integrating multiple events using a time-gated, boxcar averager and (2) reduce all external competing sources of thermal flux generated by the measurement itself.
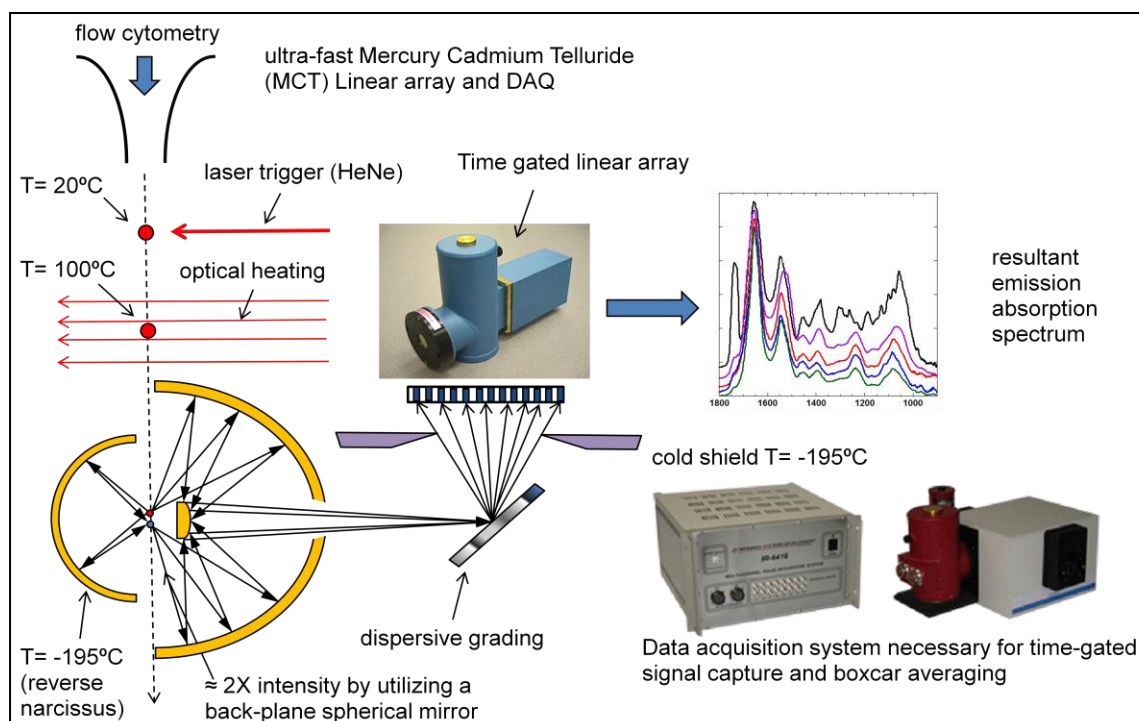
Figure 4. Simple schematic showing the free-flowing particle arrangement, which includes the trigger and heating lasers, emission signal capture optics, and a high-speed dispersive spectrometer.

The first way of optimizing signal capture (while reducing noise) is to properly know "when" and "where" the test particle is with respect to focal point of the collection optics. We used a gold-coated Schwarzschild objective, with a numeric aperture (NA) of 0.5 as our primary collection optic (figures 5 and 6). Proper signal gating was accomplished by using two focused diode lasers (operating at 635 and 670 nm) that intersect exactly at the focal point of the Schwarzschild objective. When the particle passes through the intersection point, light is scattered from the particle and is detected by a set of band-filtered Hamamatsu miniature photo-multiplier tubes (PMTs), where one is filtered to detect only the 625-nm light and the other is filtered to detect the 670-nm light. Exact triggering is further enhanced by using two fast optics and a variable aperture in the PMT module, which served to allow only rays associated with optimal particle positioning to trigger the event (figure 7). The trigger signal is then amplified and fed into a Nuclear Instrumentation Module (NIM) logic board and only when simultaneous signals from both PMTs are received is a main trigger signal sent to the data acquisition device (DAQ).

TOP VIEW

Band filtered photomultiplier
(PEM) detector

Schwarzschild objective

Dispersive spectrometer
32 element MCT array

Spherical reflector

focused
635 nm laser
(position trigger)

focused
670 nm laser
(position trigger)

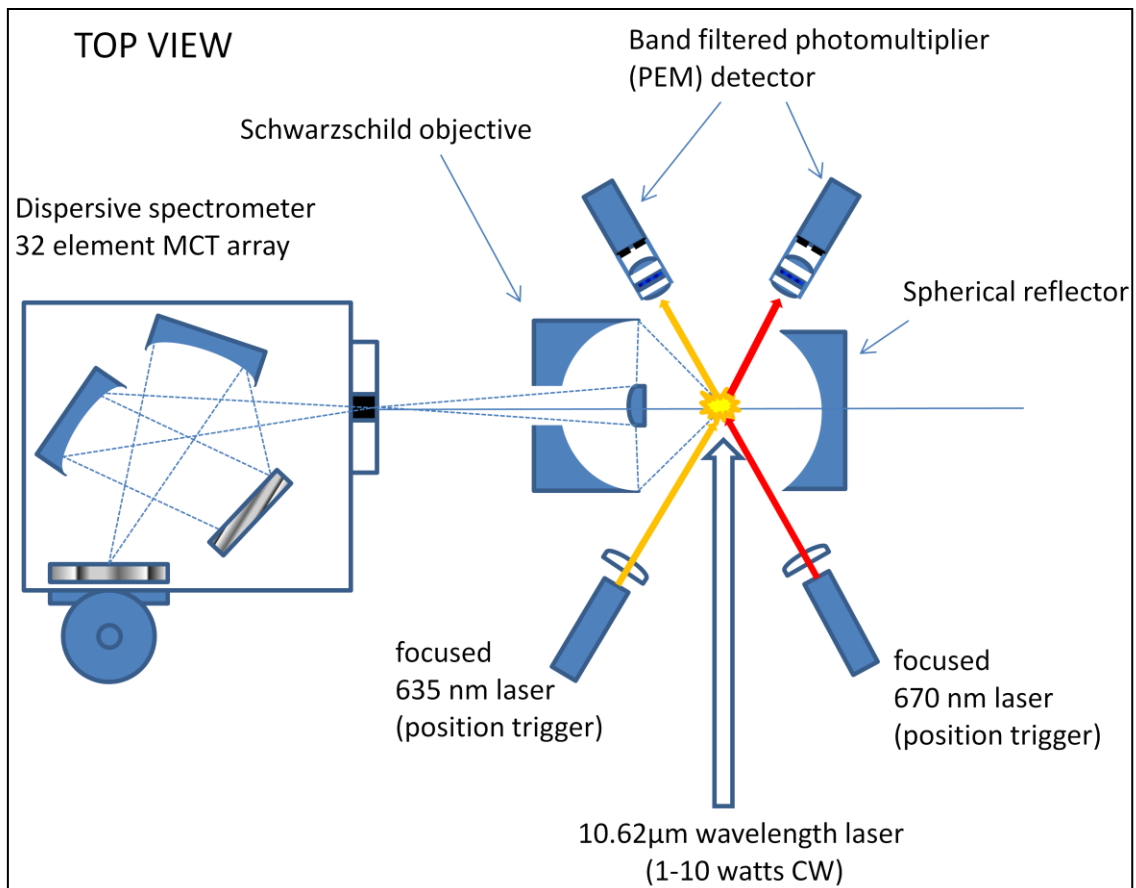10.62µm wavelength laser
(1-10 watts CW)

Figure 5. Top-view of the emission capture instrumentation including collection optics, trigger and heating lasers and a high-speed dispersive spectrometer.
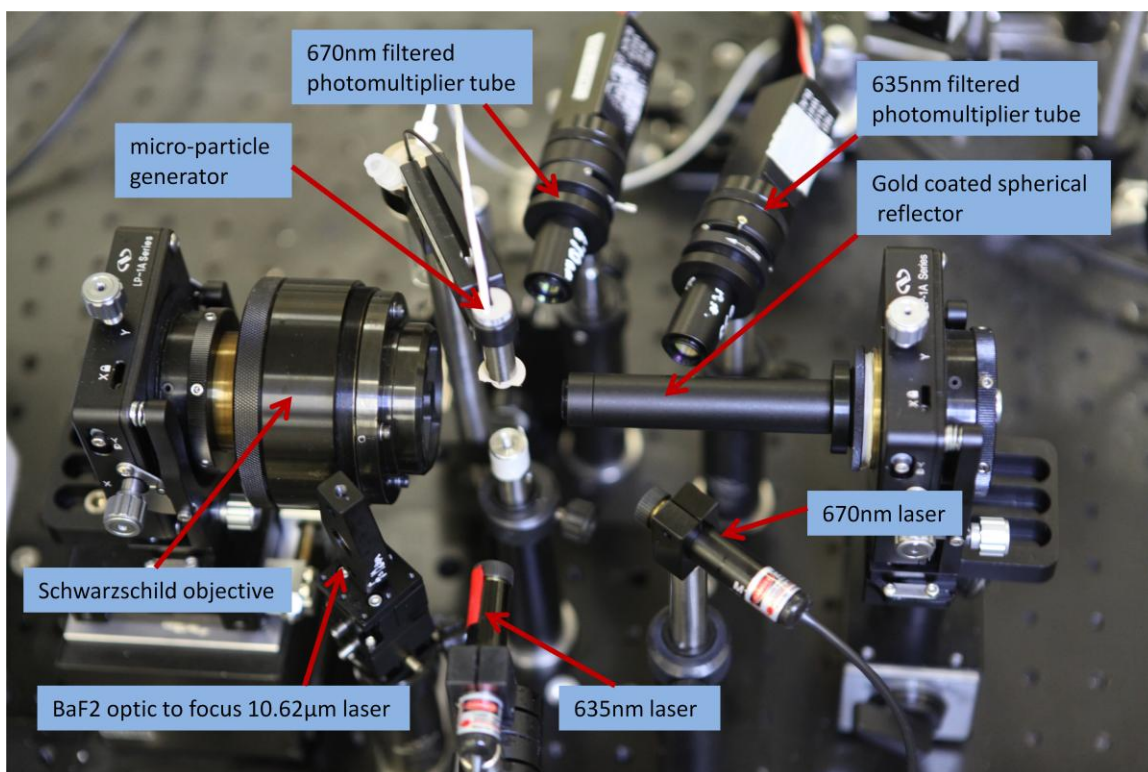
Figure 6. Photograph of the actual single particle thermal emission spectroscopy system highlighting all important components.
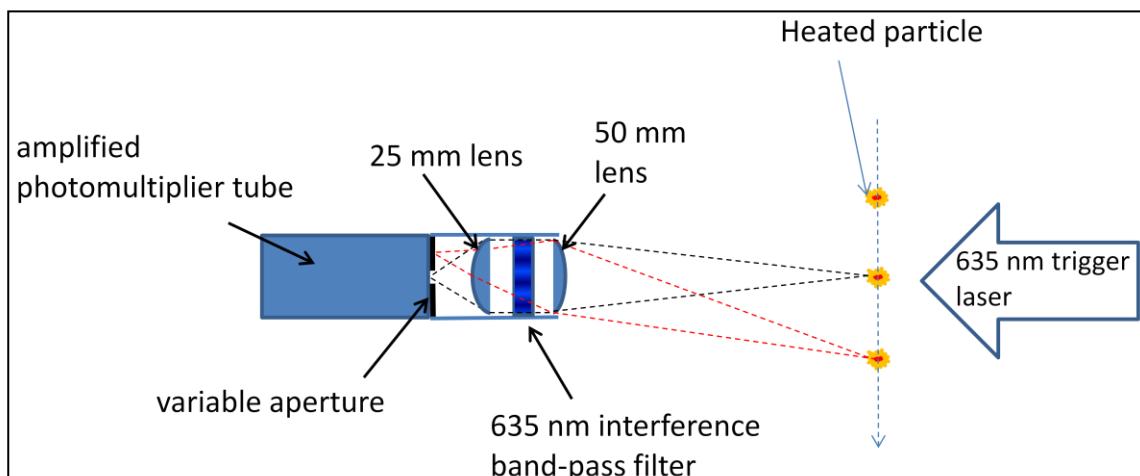
Figure 7. Diagram showing PMT collection optics for precise trigging.

It should be noted that issues arose with the signal capture and integration process due to limitations imposed by preset maximum time periods for the integration gate and the way the system conducted a baseline subtraction. Although not critical, it did take us several weeks to understand the problem and make the appropriate adjustments. Initially, we had hoped to troubleshoot the system using as large a particle as possible since larger particles would yield

stronger signals. The generation of large controlled droplets was accomplished by using a peristaltic pump to inject a set flow-rate of liquid mineral oil into a heated hypodermic needle. Heated mineral oil droplets could be produced at varying rates and sizes depending on the pump flow-rate and needle temperature. However, attempts capture and boxcar integrate the resulting emission signal failed miserably for this large diameter class of particles.

The problem arose for large particles because the amount of time the particle was being sampled by the Schwarzschild objective was longer than the maximum integration period of the DAQ, i.e., 1000 μs. A schematic showing the importance of proper signal bracketing is shown in figure 8. The bottom trace in figure 8 shows what happens when the signal event is much longer that the maximum signal integration gate. For very large particles, we were properly integrating our time gate prior to the signal being present, but because the particle was so large (took more time to pass through the probe region) we ended up stopping the gate while the signal was still present, as shown in the bottom case in figure 8.
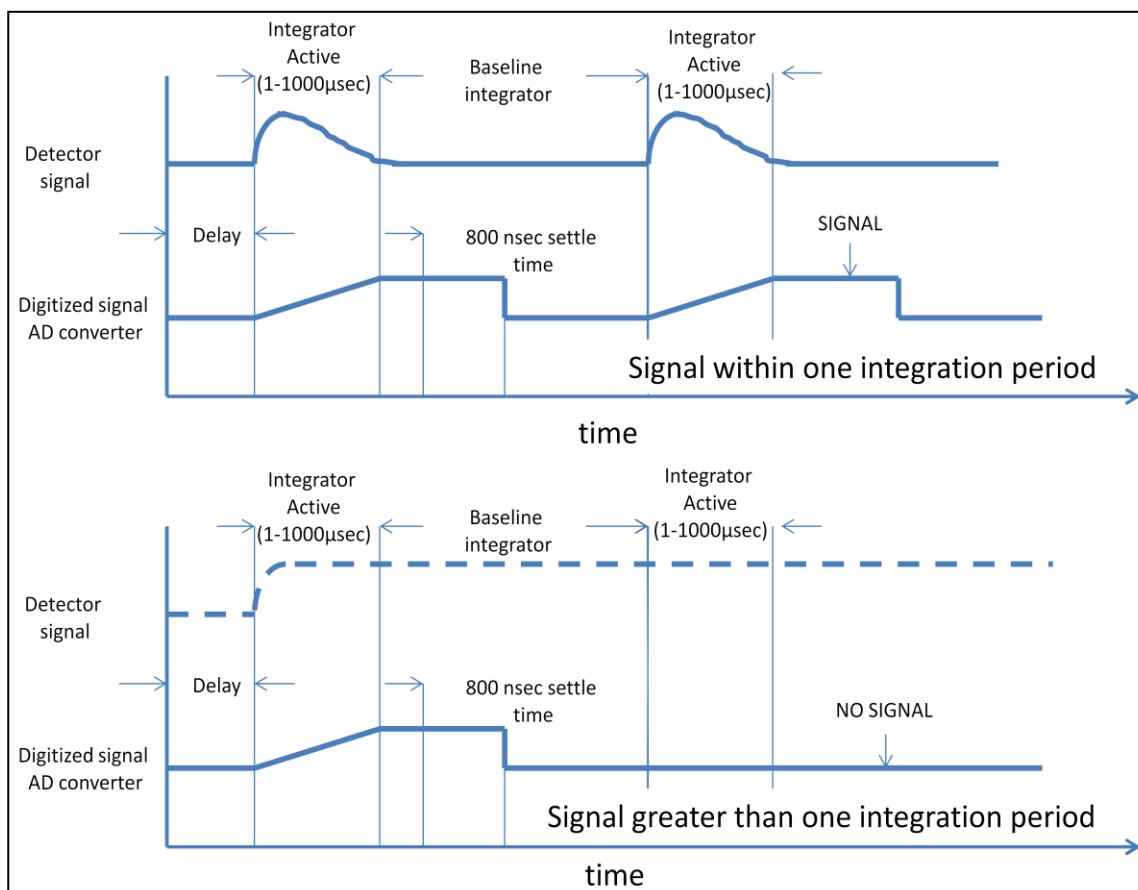

Figure 8. Timing diagram showing proper signal bracketing (top), and loss of signal encountered when the time event is too long (bottom).

11

The way the boxcar integrator conducts the baseline subtraction for this particular system is to calculate the difference in the value of the signal after the gate is closed (no radiant flux) from the signal recorded while the particle is present. Because there was signal present when there should not have been any, the net difference was zero and the DAQ never reset, resulting in no signal being recorded. We therefore had to generate an event that was less than the 1000-µs limit. To accomplish this, we had to choose to either increase the particle's velocity or reduce the size of the particle. Because our ultimate goal was to show results for particles in the 1–20 µm range, we elected to work with smaller particles. To generate smaller droplets, a Microdrop Technologies, Inc., generator (model MD-K-140-010) was inserted into the setup (see figure 6).

The next task was to reduce or eliminate as many sources of ambient thermal radiation in the 3–10 µm range as possible. Fortunately, this aspect was fairly straightforward. For the imaging spectrometer used in this study, i.e., a Horiba Triax 190, we positioned all radiometric capture optics, mirrors, and apertures so that only rays defined by the cold-shield surrounding the liquid nitrogen (LN_2) cooled MCT linear array were allowed to propagate from the particle to the 32-element detector array. Additionally, the internal compartment of the spectrometer was examined for obvious sources of thermal radiation using a microbolometer long-wave IR (LWIR) camera, and results showed several surprisingly large regions of radiant flux that were being generated by the electronics inside the spectrometer (figure 9). After inspection, these sources were eliminated by either disconnecting unnecessary electrical components or shielding the components using IR-reflecting Mylar.

To enhance the signal further, a spherical concave mirror was positioned behind the target particle so that the focal point of the mirror was coincident with particle (see figures 5 and 6). By properly positioning a spherical mirror slightly off-axis with respect to a point source, one can effectively double the apparent intensity received by the detector. In addition, the spherical mirror reduced the background that the particle is imaged against by reflecting back the cold source image of the liquid nitrogen (LN_2)-cooled MCT array.
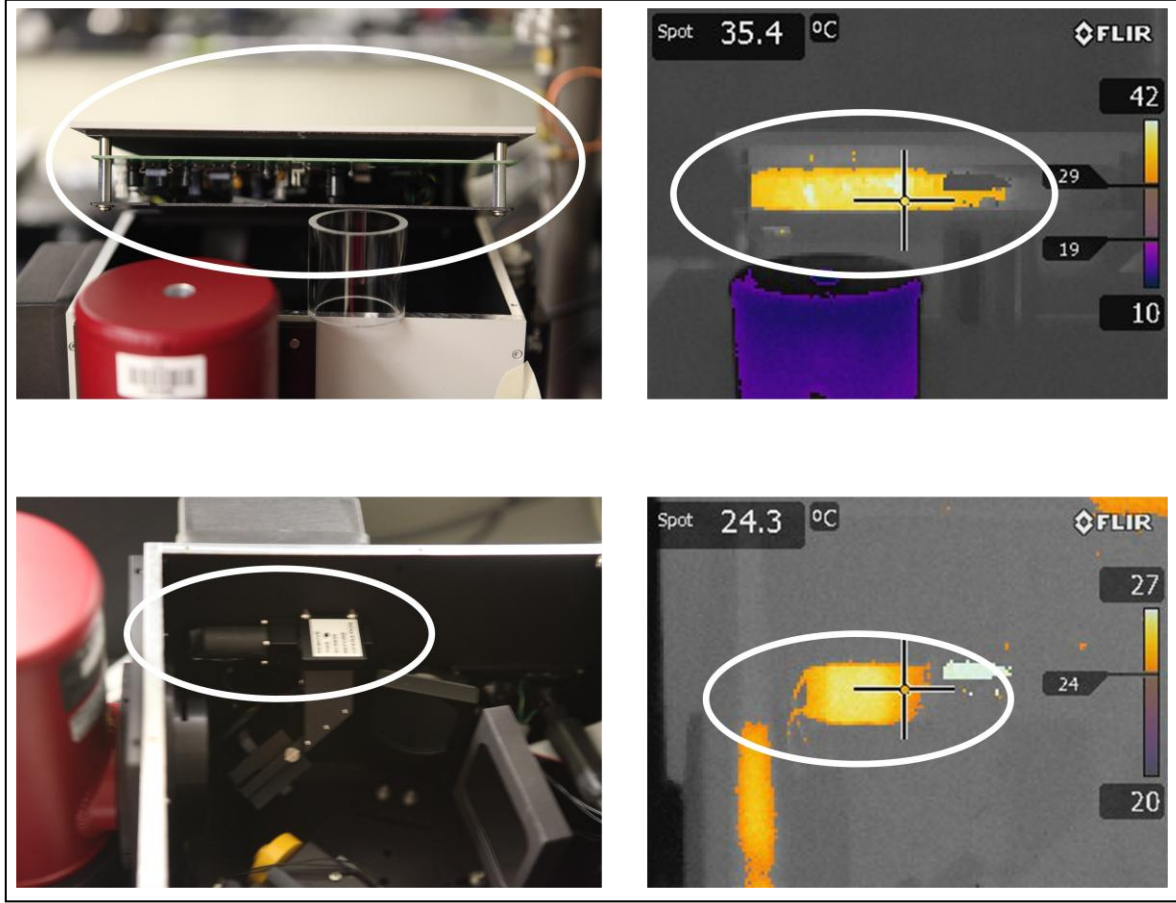
Figure 9. Inspection of ambient thermal sources within the spectrometer using a thermal imaging camera.

4. Results

To resolve the emission spectra, we used a Horiba Triax 190 imaging dispersive spectrometer. This compact imaging spectrometer (focal length 0.19 m) is based on a modified cross Czerny-Turner design, which produced an f/# value of 3.9. Dispersive gratings were switched out using a computer control mechanical turret. Blaze angles for the gratings used here were at 4000, 6000, and 9000 nm, which yielded optical dispersion values of 4.14, 12.46, and 12.41 nm/pixel, respectively. Based on the 32-element MCT linear array used to detect the dispersed emission, the maximum spectral band that could be resolved at any one grating potion was $\Delta\lambda=0.40$ μm.

With such a small spectral window of 0.4 μm per grading position, it was useful to know exactly where to position the grating in order to detect a particular emission/absorption feature. To acquire this information, we measured the transmission spectra from 3–12 μm for varying thin

13

film thicknesses of the test mineral oil using a specially machined cell and a modified Bomem emission Fourier transform infrared (FTIR) spectrometer (*26*). The resulting transmission spectra were converted into units of absorbance and is shown in figure 10.
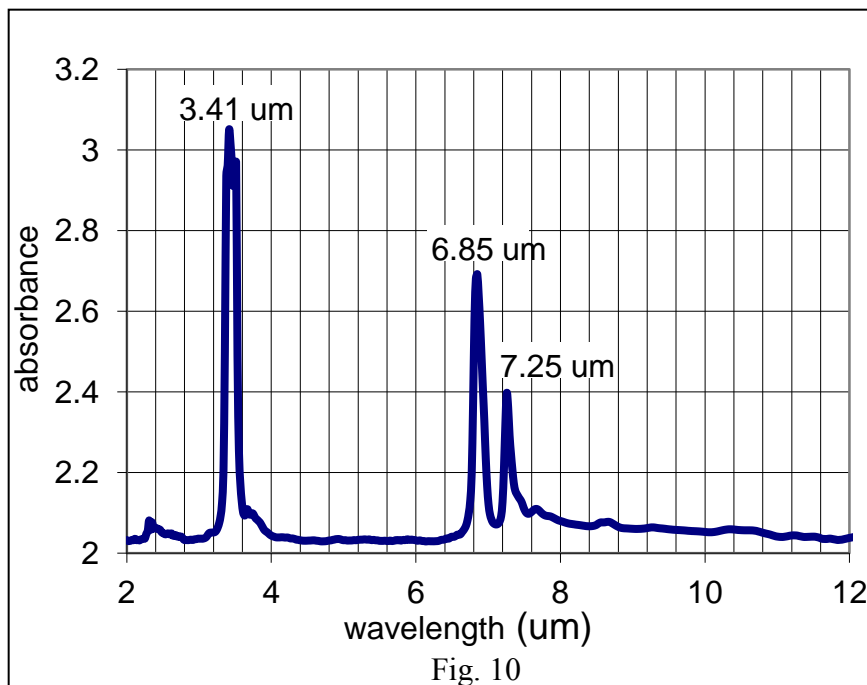

Fig. 10

Figure 10. Measured FTIR absorbance spectra for mineral oil.

Single particle emission tests were conducted over a multiday period in which the grading position was set to a specific center wavelength based on the results shown in figure 10. The particular Microdrop particle generator used here allowed for sample heating up to a temperature of 80 °C in order to reduce viscosities for vicious fluids (like mineral oil) to levels appropriate for controlled micro-drop generation. The Microdrop dispenser head uses piezo-driven inkjet printing technology. The integrated piezo actuator induces a shock-wave into the fluid contained in the head, which causes a droplet to be emitted from the nozzle. For our 75-µm-diameter orifice, the system generated particles in the 75–90 µm range at externally triggered rates between 1 to 2000 Hz. For this study, we used a nominal rate of 15 Hz, which produced measured particle velocities on the order of 2–3 m/s.

Optical heating was achieved using a Universal Inc. (model URL-10), 10-W continuous wave (CW) CO_2 laser, which was linearly polarized. Laser intensity was controlled by a series of IR neutral density (ND) filters mounted in series with a barium fluoride (BaF_2) wire-grid polarizer. The attenuated laser was precisely directed and focused to a location approximately 1.0 mm above the focal point of the Schwarzschild objective. Because we are using an "imaging" spectrometer, an object focused at the slit of spectrometer will be exactly imaged in the detector

plane, with a magnification value of 1. Since the individual pixel dimension for the MCT array was 0.5 mm (H) x 0.2 mm (W), the optimum slit width for maximum radiometric throughput was set to 0.2 mm.

Once the MCT array is cooled to the LN_2 temperature of 79 K, particle generation and signal capture was started. Before each run a baseline signal was acquired. The baseline signal records the average ambient radiance level generated by the entire optical system before the heated particle is present. This value is stored and subtracted from the radiance levels when the particle is present. Once the baseline is established, the CO_2 laser is turned on and focused to the steam of small particles being generated by the Microdrop device. Each time a particle intersects both trigger lasers, a transistor-transistor logic (TTL) signal is sent to the DAQ, which starts the acquisition of the time-gated signal. For this particular setup, the time-gate was set to 50 μs, which allowed for proper bracketing of the signal as shown in figure 8. Typical sample periods necessary to capture 1000 scans ranged was approximately 1 min for a particle generation rate of 15 Hz.

The resultant emission spectra are shown in figures 11 and 12. Figure 11 shows the emission spectra for range surrounding the first major absorption band at 3.41 μm shown in figure 10. This was accomplished by positioning the 4-μm blazed grating at a center wavelength of 3.43 μm. The emission spectra shown in figure 12 was produce during two separate sessions in which the 6-μm blazed grating was used and rotated from 6.90 μm (left half of the spectra) to 7.20 μm (right half of the spectra) in order to span a wavelength range large enough to include both absorption bands at 6.85 and 7.25 μm shown in figure 10.
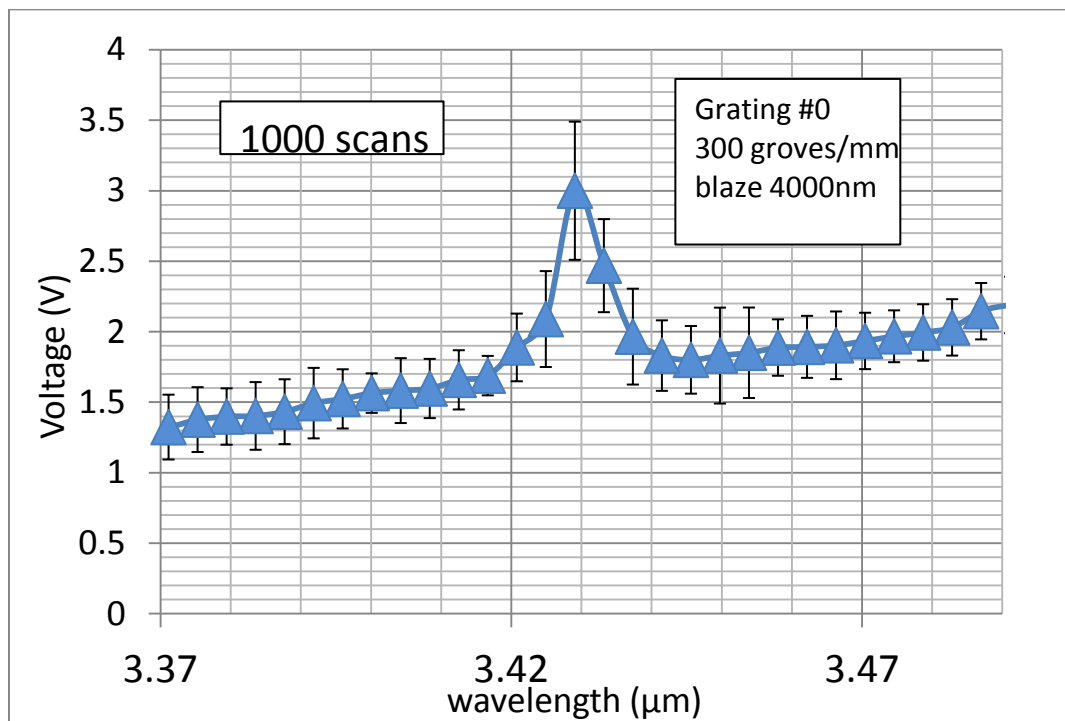

Figure 11. Measured spectral emission for the 4000-nm blazed grating from an optically heated 80-μm-diameter size droplet of mineral oil.
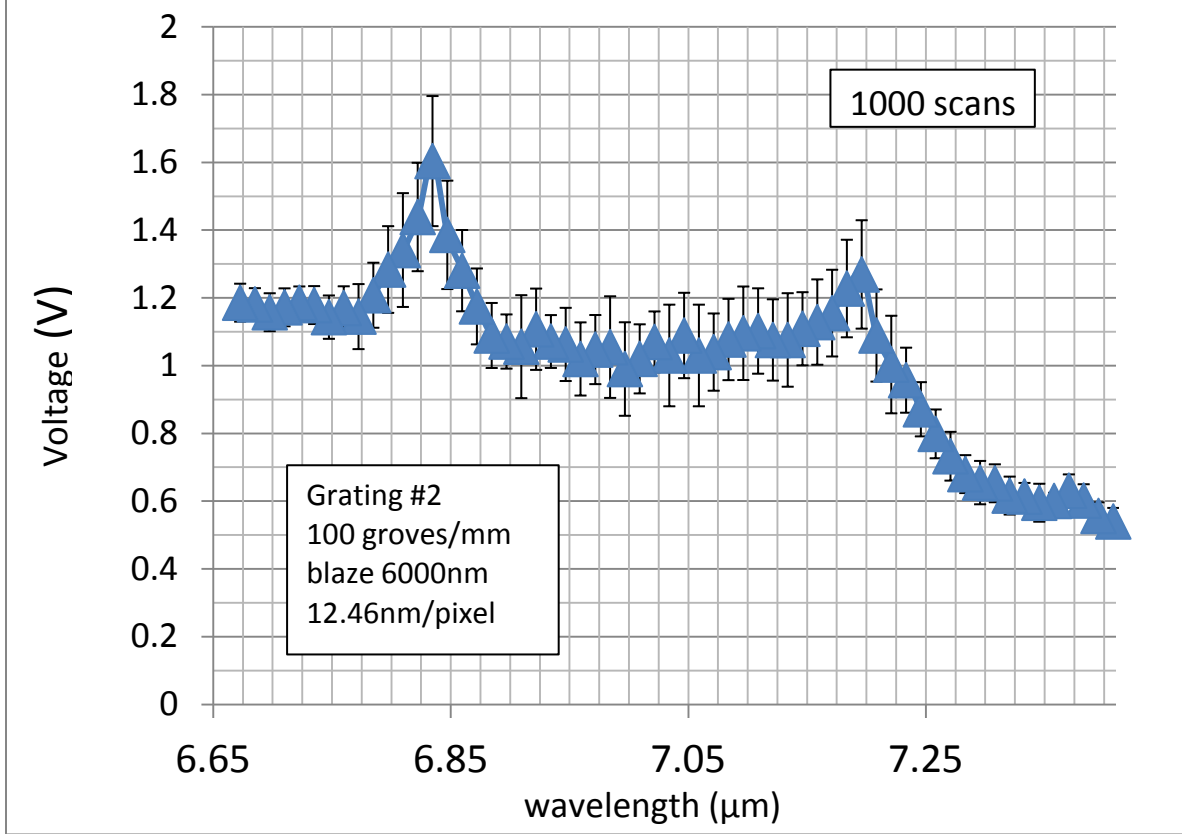
Figure 12. Measured spectral emission for the 6000-nm blazed grating, from an optically heated 80-µm-diameter size droplet of mineral oil.

As one can see the basic absorption characteristics shown in figure 10 are represented in the measure thermal emission spectra for the heated droplet. Although the overall peak locations between the absorption and emission spectra compare well, the transition between peaks appears dampened in the emission spectra. This is not entirely unexpected since the measured emission is product of the material's spectral emissivity, $\varepsilon(\lambda)$, and the Planck function, $R_b(\lambda, T_p)$, see equation 1. As the temperature of the material rises, the Planck function plays a larger role in the form of the overall thermal emission spectra. Again we have assumed that the temperature increase is such that the spectral emissivity, $\varepsilon(\lambda)$, remains relatively temperature independent.

5. Conclusion

In summary, we have shown that one can infer distinct and identifiable spectral absorption characteristics by examining the measured thermal emission that is produced when a single aerosol particle is optically heated. We are optimistic that the approach and techniques developed for this proof-of-concept study will yield similar results when applied to a larger set of biologically derived materials, e.g., pollen, amino acids, proteins, bacterial endospores, etc. We

intend to develop this approach further once we receive our BL1 safty certification for our laboratory. We hope to show that the additional information inherent in a measure of single particle emission will be of value in developing future systems designed to detect the presence of harmful BW agents.

6. References

1. Pan, Y.-L.; Hill, S. C.; Coleman, M. Photophoretic Trapping of Absorbing Particles in Air: Measurement of their Single-particle Raman Spectra. *Optics Express* **2012**, *20* (5), 5325–5334.

2. Windom, B. C.; Diwakar, P. K.; Hahn, D. W. Dual-pulse Laser Induced Breakdown Spectroscopy for Analysis of Gaseous and Aerosol Systems: Plasma-analyte Interactions. *Spectrochimica Acta Part B: Atomic Spectroscopy* **July 2006**, *6* (7), 788–796.

3. Hahn, D. W.; Lunden, M. M. Detection and Analysis of Particles by Laser-Induced Breakdown Spectroscopy. *Aerosol Sci. and Tech*. **2000**, *33* (1), 30–48.

4. Kaye, P.; Stanley, W.; Hirst, E.; Foot, E. Single Particle Multichannel Bio-aerosol Fluorescence Sensor. *Optics Exp.* **2005**, *13* (10), 3583–3593.

5. Pan, Y.-L; Hill, S.; Pinnick, R.; House, J.; Flagan, R.; Chang, R. Dual-excitation-wavelength Fluorescence and Elastic Scattering for Differentiation of Single Airborne Pollen and Fungal Particles. *Atmos. Envoi.* **2011**, *45,* 1555–1563.

6. Hairston, P. P.; Ho, J. Design of an Instrument for Real-Time Detection of Bioaerosols using Simultaneous Measurement of Particle Aerodynamic Size and Intrinsic Fluorescence. *J. Aerosol Sci.* **1997**, *28*, 471–482.

7. Boutou, V.; Favre, C.; Hill, S. C.; Pan, Y. L.; Chang, R. K.; Wolf, J. P. Backward Enhanced Emission from Multiphoton Processes in Aerosols. *Appl. Phys. B* **2002**, *75*, 145–152.

8. Weigel, T.; Shulte, J.; Schweiger, G. Inelastic Scattering by Particles of Arbitrary Shape. *J. Opt. Soc. Am. A* **2006**, *23*, 2797–2802.

9. Rytov, S. The Theory of Electrical Fluctuations and Thermal Radiation, (English Translation by U.S. Air Force Cambridge Research Center, Bedford, MA, Rep. AFCRC-TR-59-162). USSR Academy of Science, Moscow, 1953.

10. Bekefi, G. *Radiation Processes in Plasmas*; John Wiley & Sons, New York, 1966.

11. Filippov, A. V.; Markus, M. W.; Roth, P. In-situ Characterization of Ultrafine Particles by Laser-induced Incandescence: Sizing and Particle Structure Determination. *J. Aerosol Sci.* **1999**, *30* (1), 71–87.

12. Van De Hulst, H. C. *Light Scattering by Small Particles*; John Willey Press, New York, 1957.

13. Bohren, C. F.; Huffman, D. *Absorption and Scattering of Light by Small Particles*; John Wiley Press, New York, 1983.

14. Filippov, A. V.; Roth, P. Laser-induced Incandescence Method for Ultrafine Particle Sizing. *J. Aerosol Sci.* **1996**, *27* (1), s699–s700.

15. Williams, M.; Loyalka, S. *Aerosol Science: Theory and Practice*; Pergamon Press, Oxford, 1991.

16. Carslaw, H. S.; Jaeger, J. C. *Conduction of Heat in Solids*; Oxford Press, Oxford, (1959).

17. Davis, E. J. A History of Single Particle Levitation. *Aerosol Sci. Tech.* **2007**, *26* (3), 212–254.

18. Ashkin, A. Acceleration and Trapping of Particles by Radiative Pressure. *Phys. Rev. Lett* **1970**, *24* (4), 156–159.

19. Huisken, J.; Stelzer, E. Optical Levitation of Absorbing Particles with a Nominally Gaussian Laser Beam. *Opt. Lett.* **2002**, *2* (14), 1223–1225.

20. Ashkin, A. Acceleration and Trapping of Particles by Radiation Pressure. *Phys. Rev. Lett.* **1970**, *24*, 156–159.

21. Shvedov, V. G.; Hnatovsky, C.; Rode, A.; Krolikowski, W. Robust Trapping and Manipulation of Airborne Particles with a Bottle Beam. *Opt. Exp.* **2011**, *19*, 18.

22. Shvedov, V. G.; Desyatnikov, A. S.; Rode, A. V. Optical Vortex Beams for Trapping and Transport of Particles in Air. *Appl. Phys. A.* **2010**, *100*, 327–331.

23. Pan, Y.-L.; Hill, S. C. *Raman Spectra of Individual Airborne Particles*; ARL-MR-0806; U.S. Army Research Laboratory: Adelphi, MD, January 2012.

24. Pan, Y.-L.; Hill, S.; Pinnick, R.; House, J.; Flagan, R.; Chang, R. Dual-excitation-wavelength Fuorescence and Elastic Scattering for Differentiation of Single Airborne Pollen and Fungal Particles. *Atmos. Envoi.* **2011**, *45*, 1555–1563.

25. Pan, Y.; Bowersett, J.; Hill, S.; Pinnick, R.; Chang, R. *Nozzles for Focusing Aerosol Particles*; ARL-TR-5026; U.S. Army Research Laboratory: Adelphi, MD, October 2009.

26. Gurton, K. P.; Felton, M.; Dahmani, R.; Ligon, D. In situ Infrared Aerosol Spectroscopy for a Variety of Nerve Agent Simulants using Flow-through Photoacoustics. *Applied Optics* **2007**, *46* (25), 6323–6329.

List of Symbols, Abbreviations, and Acronyms

2-D	two-dimensional
BaF_2	barium fluoride
BG	*bacillus subtilis*
BL1	bio-safety level 1
BW	biological warfare
CO_2	carbon dioxide
CW	continuous wave
DAQ	data acquisition device
FTIR	Fourier transform infrared
HeNe	helium neon
IR	infrared
LIBS	laser induced breakdown spectroscopy
LN_2	liquid nitrogen
LWIR	long-wave IR
MCT	mercury cadmium telluride
NA	numeric aperture
ND	neutral density
NIM	Nuclear Instrumentation Module
PMTs	photo-multiplier tubes
TTL	transistor-transistor logic

NO. OF
COPIES   ORGANIZATION

1   ADMNSTR
ELEC   DEFNS TECHL INFO CTR
         ATTN DTIC OCP
         8725 JOHN J KINGMAN RD STE 0944
         FT BELVOIR VA 22060-6218

5 PDFS   US ARMY RSRCH LAB
         ATTN IMAL HRA MAIL & RECORDS MGMT
         ATTN RDRL CIO LL TECHL LIB
         ATTN RDRL CIE S
         KRISTAN P. GURTON
         MELVIN FELTON
         YONGLE PAN
         ADELPHI MD 20783-1197

INTENTIONALLY LEFT BLAND